JGR Solid Earth

RESEARCH ARTICLE
10.1029/2019JB017905

Key Points:
- Granitic rocks sheared at seismic slip velocities and low normal stress show double-strengthening friction evolution before final weakening
- Particle size distribution constrained by in situ synchrotron analysis shows the presence of additive ultrafine quartz grains
- The re-strengthening was due to viscous frictional melts by quasi-equilibrium melting and the Gibbs-Thomson effect on quartz grains

Correspondence to:
L.-W. Kuo,
liweikuo@ncu.edu.tw
liweikuo@gmail.com

Citation:
Hung, C.-C., Kuo, L.-W., Spagnuolo, E., Wang, C.-C., Di Toro, G., Wu, W.-J., et al (2019). Grain fragmentation and frictional melting during initial experimental deformation and implications for seismic slip at shallow depths. *Journal of Geophysical Research: Solid Earth*, *124*. https://doi.org/10.1029/2019JB017905

Received 24 APR 2019
Accepted 24 OCT 2019
Accepted article online 15 NOV 2019

Chien-Cheng Hung and Li-Wei Kuo contributed equally to this work.

Grain Fragmentation and Frictional Melting During Initial Experimental Deformation and Implications for Seismic Slip at Shallow Depths

Chien-Cheng Hung[1,2], Li-Wei Kuo[1], Elena Spagnuolo[3], Chun-Chieh Wang[4], Giulio Di Toro[3,5], Wen-Jie Wu[1], Jia-Jyun Dong[6], Wayne Lin[7], Hwo-Shuenn Sheu[4], En-Chao Yeh[8], and Pei-Shan Hsieh[7]

[1]Department of Earth Sciences, National Central University, Taoyuan, Taiwan, [2]Now at Earth Simulation Laboratory, Department of Earth Sciences, Utrecht University, Utrecht, The Netherlands, [3]Istituto Nazionale di Geofisica e Vulcanologia, Rome, Italy, [4]National Synchrotron Radiation Research Center, Hsinchu, Taiwan, [5]Dipartimento di Geoscienze, Università di Padova, Padua, Italy, [6]Graduate Institute of Applied Geology, National Central University, Taoyuan, Taiwan, [7]Industrial Technology Research Institute, Hsinchu, Taiwan, [8]Department of Earth Sciences, National Taiwan Normal University, Taipei, Taiwan

Abstract During seismic slip, the elastic strain energy released by the wall rocks drives grain fragmentation and flash heating in the slipping zone, resulting in formation of (nano)powders and melt droplets, which lower the fault resistance. With progressive seismic slip, the frictional melt covers the slip surface and behaves as a lubricant reducing the coseismic fault strength. However, the processes associated to the transition from grain fragmentation to bulk frictional melting remain poorly understood. Here we discuss in situ microanalytical investigations performed on experimentally produced solidified frictional melts from the transition regime between grain fragmentation and frictional melting. The experiments were performed on granitic gneiss at seismic slip rates (1.3 and 5 m/s), normal stresses ranging from 3 to 30 MPa. At normal stresses <12 MPa, the apparent friction coefficient μ_{app} (shear stress versus normal stress) evolves in a complex manner with slip: μ_{app} decreases because of flash weakening, increases up to a peak value μ_{p1} ~0.6–1.0, slightly decreases and increases again to a second peak value μ_{p2} ~0.44–0.83, and eventually decreases with displacement to a steady-state value μ_{ss} ~0.3–0.45. In situ synchrotron observations of the solidified frictional melt show abundance of ultrafine quartz grains before μ_{p2} and enrichment in SiO_2 at μ_{p2}. Because partial melting occurs on the ultrafine quartz grains and, as a consequence, it suggested that the second re-strengthening (μ_{p2}) is induced by the higher viscosity of the melt due to its enrichment in Si from melting of the ultrafine quartz grains derived from grain fragmentation.

1. Introduction

Numerous physical and chemical processes have been theoretically and experimentally proposed to justify fault lubrication during seismic slip, for example, flash heating (Beeler et al., 2008; Goldsby & Tullis, 2011; Rice, 2006), powder lubrication (Han et al., 2010; Reches & Lockner, 2010), frictional melting (Di Toro et al., 2006; Spray, 2005), silica gel formation (Di Toro et al., 2004), elastohydrodynamic lubrication (Brodsky & Kanamori, 2001; Cornelio et al., 2019), grain size- and temperature-dependent processes (De Paola et al., 2015; Green et al., 2015; Rowe et al., 2019; Spagnuolo et al., 2015), and thermal decomposition (Collettini et al., 2013; Han et al., 2007). In particular, on a fault patch in silicate-built rocks, flash heating and melting (Goldsby & Tullis, 2011), or grain fragmentation of the rock (Chen et al., 2017a; De Paola et al., 2015; Green et al., 2015; Rowe et al., 2019; Spagnuolo et al., 2015) may occur during the initial stages of seismic slip at the passage of the earthquake rupture propagation front. With progressive slip, the continuously generated melt droplets can accumulate to form a continuous melt layer possibly resulting in melt lubrication (Shimamoto, 2005; Spray, 1995). Therefore, studies on powder generation, flash heating and melting, and the formation of a continuous melt layer provided criteria for understanding fault lubrication (Reches & Lockner, 2010; Chen, Madden, & Reches, 2017a; Spray, 1995, 2005; Di Toro Hirose, Nielsen, Pennacchioni, et al., 2006; Rice, 2006; Beeler et al., 2008; Goldsby & Tullis, 2011).

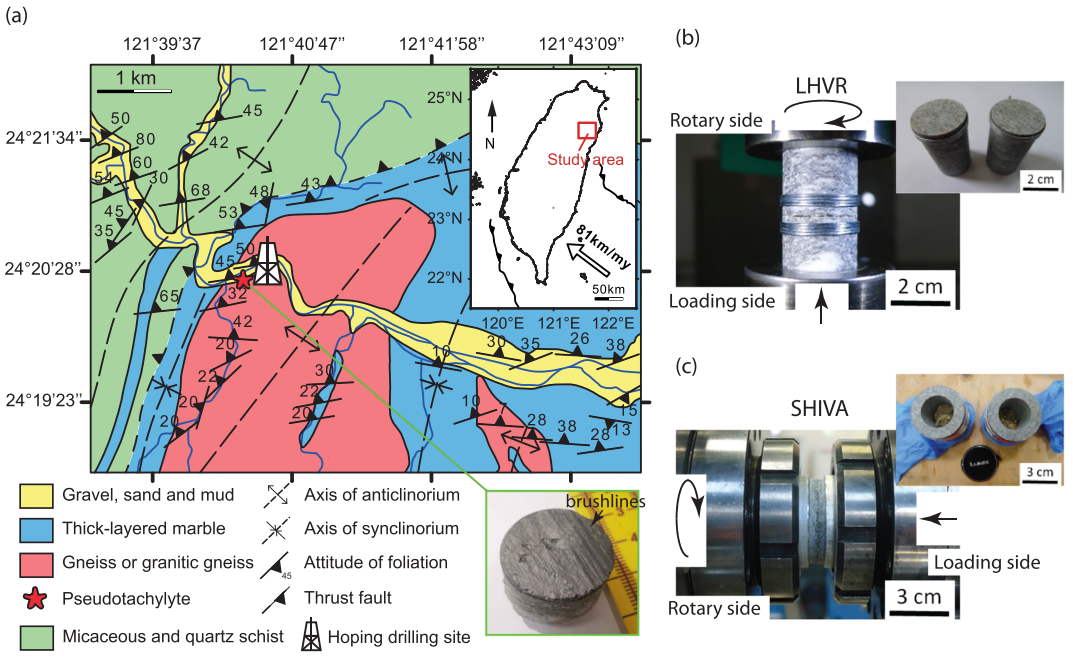

Figure 1. (a) Geological setting of the Hoping area with complex tectonic structures. The inset box shows the location of the Hoping area in northeast Taiwan. The study area consists mainly of marble, granitic gneiss, and schist. The Hoping pseudotachylyte (red star) and its surface structure "brushlines" (green box; the surface was coated by Pt for SEM analysis) and the Hoping borehole are located alongside the Hoping River and are hosted in granitic gneiss. The attitude of foliation is mostly parallel or subparallel to the direction of fold axis. (b and c) Specimen assembly for LHVR and SHIVA. Note that the specimen size for LHVR is 25 mm in diameter and for SHIVA, the outer diameter is 50 mm and the inner diameter is 30 mm. Specimens were bound with iron wires and jacketed with aluminum rings for LHVR and SHIVA, respectively.

However, the transition between fault rock comminution and frictional melting remains unclear. More relevantly, how do the associated frictional properties derived from both fault comminution and frictional melting affect the fault strength during fault rupture is not well-constrained. Here we address these questions by conducting rock friction experiments on granitic gneiss at seismic rates and further discuss how the presence of fragmented grains and the chemical evolution of the friction melt influence the frictional behavior of the experimental fault.

2. Materials and Methods

2.1. Starting Materials

The exhumed pseudotachylyte-bearing fault, which crosscuts the granitic gneiss of the Tananao Metamorphic Complex (TMC), crops out in the Hoping area, northeast Taiwan (Chu et al., 2012; Figure 1a). The fault zone rocks are mainly cataclasites and mylonites overprinted by pseudotachylytes. Pseudotachylytes were generated at depths >4 km about 1.6 Ma ago (Chen et al., 2017) in faults accommodating displacements by up to 220 mm (corresponding to earthquakes of M_W 6.4 ± 0.4 if all the displacement would be associated to a single seismic slip event; Korren et al., 2016). Pseudotachylytes form vein and injection veins networks that intrude the host granitic gneiss, and they were used to infer earthquake source parameters (e.g., slip vectors (Korren et al., 2016) and brushlines (Ferré et al., 2016)). We used the granitic gneiss from the Hoping borehole cores drilled by the Industrial Technology Research Institute (ITRI) as the starting materials for the rotary shear experiments (Figures 1b and 1c). The mineral composition of the core granitic gneiss is 35–40% quartz, 15–25% feldspar, 20–25% micas (muscovite dominant), and 5–10% other accessory minerals (estimated by optical microscope analysis of thin sections). This estimated composition is similar to the modal content of the granitic gneiss cropping out in the area with 30–35% quartz, 20–25% feldspar, 30–35% micas (both muscovite and biotite), 3–5% clinozoisite-epidote and titanite, and 2% of other accessory minerals

Table 1
Normalized average chemical composition of the granitic gneiss, glass matrix at four states, and chemically-based melt viscosity. Noted that the bulk composition of the granitic gneiss is cited from Kuo (2016) which using XRF to analyze four rock samples.

	n	Si	Al	Mg	Ca	Na	K	Ti	Fe	Mn	P	Total	Estimated melt viscosity range (Pa s)
Granitic gneiss (Kuo, 2016)	4	65.6 ± 2.42	16.2 ± 0.67	1.8 ± 0.13	2.8 ± 0.44	2.7 ± 0.05	3.8 ± 0.28	1.0 ± 0.14	5.8 ± 1.21	0.1 ± 0.00	0.2 ± 0.05	100.00	–
State A (LHVR0484)	39	58.3 ± 5.87	18.6 ± 2.64	2.1 ± 0.39	4.2 ± 0.77	2.9 ± 0.51	6.2 ± 0.82	0.6 ± 0.63	7.2 ± 1.25	–	–	100.00	$10^{8.0–3.1}$
State B (LHVR0552)	40	53.0 ± 3.47	20.4 ± 1.35	2.6 ± 0.46	4.9 ± 1.12	2.7 ± 0.85	7.1 ± 0.63	1.0 ± 0.59	8.4 ± 1.48	–	–	100.00	$10^{7.7–2.7}$
State C (LHVR0452)	39	61.3 ± 5.91	17.5 ± 2.63	2.2 ± 0.42	4.4 ± 1.22	3.0 ± 0.52	6.1 ± 0.92	0.2 ± 0.39	5.3 ± 1.20	–	–	100.00	$10^{8.2–3.3}$
State D (LHVR0438)	40	50.1 ± 3.02	17.2 ± 1.54	2.5 ± 0.3	13.5 ± 1.92	2.8 ± 0.31	6.3 ± 0.95	0.6 ± 1.34	7.0 ± 1.62	–	–	100.00	$10^{7.1–2.7}$

n, number of analyses.

(Chu et al., 2012). The bulk chemical composition of the granitic gneiss is also shown in Table 1. The granitic gneiss has a heterogeneous mineralogical distribution due to the presence of a foliation enriched in muscovite or in quartz and feldspar (Figures 1b and 1c). To achieve more homogenous mineralogy of the sliding surface, the samples prepared for the experiments were drilled with the long axis oblique (approximately 25° to 30°) to the gneissic foliation.

2.2. Rock Deformation Experiments

Rock deformation experiments were conducted with the low-to-high velocity rotary shear friction apparatus (LHVR) installed at the National Central University (NCU), Taiwan (Kuo et al., 2015; Yang et al., 2014), and the slow-to-high velocity apparatus (SHIVA) at the Istituto Nazionale di Geofisica e Vulcanologia (INGV, Rome), Italy (Di Toro et al., 2010). The latter was used to extend the applied normal stresses up to 30 MPa and perform an experiment under vacuum conditions.

For LHVR, the samples were solid cylinders (25-mm external diameter) which were tightly confined with iron wires (Figure 1b). For SHIVA, the samples were hollow cylinders (50-mm external, 30-mm internal diameters) which were jacketed with an external aluminum ring (Figure 1c; Niemeijer et al., 2011; Nielsen et al., 2012). To improve the alignment of two mounted samples before the experiments, for LHVR, we gently knocked the edge of the upper one until the measured uncentered degree was lower than 10 μm, and, for SHIVA, we preground the slip surface of the samples at 1 cm/s and 1 MPa (Niemeijer et al., 2011). The pregrinding lasted until the recorded torque achieved a constant value which is associated with the parallelism of the two opposite sliding surfaces.

Because of the rotary configuration of the two machines used, both slip and slip rate increase with sample radius. As a consequence, we define the equivalent slip rate V_e (Shimamoto, 2005; Shimamoto & Tsutsumi, 1994):

$$V_e = \frac{4\pi R\left(r_{ext}^2 + r_{ext}r_{int} + r_{ext}^2\right)}{3\left(r_{ext} + r_{int}\right)} \left[\frac{m}{s}\right] \quad (1)$$

where R is the revolution rate of the motor (i.e., the target R in the experiments presented here were 1,500 rpm for LHVR and 3,000 rpm for SHIVA), r_{ext} the external radius (12.5 and 25 mm for LHVR and SHIVA, respectively), and r_{int} the internal radius (0 and 15 mm for LHVR and SHIVA, respectively) of the samples (Figure 1). The experimental conditions above resulted in target V_e of 1.3 and 5 m/s for LHVR and SHIVA, respectively. Hereafter we refer to the "equivalent slip rate" as slip rate. The measured torque (T) allows us to determine the shear stress (τ) by assuming that τ is constant over the entire slip surface (Shimamoto, 2005):

Table 2
List of experiments, experimental conditions, mechanical data, and mechanically-constrained apparent viscosity.

Experiment	σ_n (MPa)	First Peak τ_{p1} (MPa)	Second peak τ_{p2} (MPa)	Average steady state τ_{ss} (MPa)	Slip velocity V (m/s)	Total slip D (m)	Acceleration/ Deceleration (m/s^2)	Melt thickness w (mm)	Apparent viscosity η_{app} (Pa S)	Clast content ϕ (%)	Apparent viscosity corrected with clasts η_c (Pa S)	Ambient condition
LHVR0484 (State A)	3	4.7	–	–	1.3	1.6	3.5	0.27	613	20	229	RH
LHVR0487 (State A)	3	2.9	–	–	1.3	1.5	3.5	–	–	–	–	RH
LHVR0534 (State B)	3	3	–	–	1.3	2.6	3.5	–	–	–	–	RH
LHVR0552 (State B)	3	3	–	–	1.3	2.7	3.5	0.33	548	18	232	RH
LHVR0452 (State C)	3	2.5	1.55	–	1.3	2.1	3.5	0.17	203	11	125	RH
LHVR0438 (State D)	3	2.8	2.5	1.5	1.3	5.7	3.5	0.23	265	20	99	RH
LHVR1097 (State D)	3	1.6	2.1	1.4	1.3	5.3	3.5	–	–	–	–	RH
LHVR0439	6	4.6	3.4	2.8	1.3	4.7	3.5	–	–	–	–	RH
LHVR0440	9	5.3	4	2.8	1.3	3	3.5	–	–	–	–	RH
LHVR0441	12	6.7	–	3.3	1.3	6	3.5	–	–	–	–	RH
LHVR0443	19	7.5	–	3.4	1.3	1.9	3.5	–	–	–	–	RH
s1286	3	3	2.4	1.6	5	7.5	6.5	–	–	–	–	Vacuum
s1289	30	12.7	–	4.7	5	1.5	6.5	–	–	–	–	RH

RH, room humidity

$$T = \int_{r_{int}}^{r_{ext}} 2\pi\tau r^2 dr = \frac{2\pi\tau}{3}\left(r_{ext}^3 - r_{int}^3\right)\ [N\ m] \tag{2}$$

Given the strong assumption of a constant shear stress over the entire slip surface, which cannot be the case as the shear stress varies with slip rate (e.g., Di Toro et al., 2011) and in the cylindrical configuration the slip rate increases with the sample radius, mechanical data obtained with hollow cylinders are more accurate than those obtained with solid cylinders. From equation (2), the friction coefficient μ is

$$\mu = \frac{\tau}{\sigma} = \frac{3T}{2\pi\sigma(r_{ext}^3 - r_{int}^3)} \tag{3}$$

Hereafter, we refer to μ as apparent friction coefficient μ_{app} for the following description.

The LHVR experiments were conducted at normal stresses of 3, 6, 9, 12, and 19 MPa, at a target slip rate of 1.3 m/s, and under room humidity conditions. The SHIVA experiments were conducted at the normal stresses of 3 and 30 MPa, respectively, and at a target slip rate of 5 m/s under both vacuum and room humidity conditions (Table 2). All mechanical data (torque, angular rotation, and axial displacement) were acquired at a frequency up to 1 and 25 kHz for LHVR and SHIVA, respectively. The friction coefficient of the granitic gneiss evolved in a complex manner with slip. Because of this, we conducted slip-stepping experiments or experiments that were stopped at the about the maximum or minimum values of the friction coefficient.

2.3. Analytical Methods

1. We impregnated the experimental products of LHVR with epoxy resin and prepared petrographic thin sections and rock slices, both cut across the diameter of the sample and perpendicular to slipping surface. The petrographic thin sections were prepared with a thickness of 30 μm, mounted on silica glass, and polished by 0.3-μm-thick alumina powder for optical and scanning electron microscopy analysis. The

thickness of rock slices were ~1 mm for in situ synchrotron X-ray diffraction (XRD) and micro-Raman spectroscopy analysis.

2. Three-lens optical microscopy (OM; Leica DMLP) coupled with an image capture system, and field emission scanning electron microscopy, coupled with an energy dispersive spectrometer (FESEM/EDX; JSM-7000F model) equipped at the National Central University, Taiwan, were used to investigate the microstructures and determine the semiquantitative chemical composition of the solidified frictional melt. For SEM-EDX, the petrographic sections were sputtered with platinum at 5-nm thickness and semiquantitatively analyzed at 15 kV with a focused beam of ~1 μm in diameter.
3. The in situ synchrotron XRD installed at the beamline BL01C2 in the National Synchrotron Radiation Research Center (NSRRC), Taiwan, was used to determine the mineral assemblages of both the solidified frictional melt and the host rock. The analyses were operated at a wavelength of 0.774910 Å, with an electron beam energy of 1.5 GeV and a beam size of 150 μm in diameter. Because of the presence of large grains (~1.0 mm in size) of quartz, the samples of gneiss, differently from the solidified frictional melts, were reduced into powders and analyzed. This prevented the presence of intensity anomalies in the XRD spectra due to the occurrence of crystals (e.g., quartz) larger than the X-ray beam (Kuo et al., 2014; Kuo et al., 2014). However, the intensity anomalies can still be observed in the results of the glass matrix owing to the presence of large survivor quartz or feldspar grains. To reduce the effect of intensity anomalies and representatively present the synchrotron XRD data, the spectra were reported as the average values of three analyses on the same sample.
4. The micro-Raman spectroscopy (Horiba Jobin Yvon UV-Vis Labram HR) at the National Taiwan Museum was used to determine the presence of water within the solidified frictional melt. We focused on the region from 100 to 4,000 cm^{-1} on the Raman spectrum. The analysis was operated with a 532-nm laser as an excitation source with a beam size of 1–2 μm in diameter under a 100X objective with a final laser power of 100 mW on the sample surface. A charged-coupled device (CCD) detector was installed in the microscope used to focus the excitation laser beam to collect the backscattered Raman signal. We collected three data of the matrix per deformed sample for the solidified frictional melt at an acquisition time of 15 s per analysis. We added the Raman spectra of pure water and quartz for comparison.
5. The synchrotron transmission X-ray microscopy (TXM) at the beamline BL01B1 (Song et al., 2007; Song et al., 2007; Yin et al., 2006) at the NSRRC, Taiwan, was used to obtain X-ray radiographies to determine the particle size distribution (PSD) of the survivor clasts hosted in the solidified frictional melt. The analysis was conducted on a 30-μm-thick sample collected from the petrographic thin sections over an area of 375 × 75 μm. The beam X-ray energy was 8 keV and the analysis had a spatial resolution of 50 nm (see Song, Chang, et al., 2007; Song, Kuo, et al., 2007).
6. The software *ImageJ* (available at https://imagej.nih.gov/ij/) was used to process the images of both the back scattering electron (BSE) and the TXM to estimate the PSD of the survivor grains within the solidified frictional melt. *ImageJ* allowed us to measure the size of quartz grains by exploiting the gray contrast between the glass matrix and the quartz grains in the BSE images (Kuo et al., 2015). On the contrary, we draw by hand the survivor grains from the TXM images due to the difficulty of the contrast identification between glass matrix and grains. By doing this, the overlapping of the survivor grains could be also clearly identified.
7. One experiment (LHVR1097) performed on granitic gneiss from the outcrop was recorded with an infrared thermal-sensing camera (thermoIMAGER TIM160, MICRO-EPSILON) to measure the temperature evolution of the experimental fault with slip. The infrared camera, integrated with the TIMConnect software, provided an instantaneous measurement of the temperature from 150 °C to 900 °C over an area of 0.6 mm in diameter at an acquisition rate of 10–500 Hz. Since the slipping zone is <0.3 mm in thickness and the temperature is measured from outside, the measured temperatures yielded a minimum estimate of the temperatures achieved in the slipping zone.

3. Results

3.1. Frictional Behavior and Temperature Evolution During Fast Shear Experiments

The mechanical data exhibit a complicated evolution of μ_{app} with slip, which varied with normal stress (Figure 2a). At slip initiation, once the static friction μ_s was overcome, μ_{app} decreased rapidly to a first

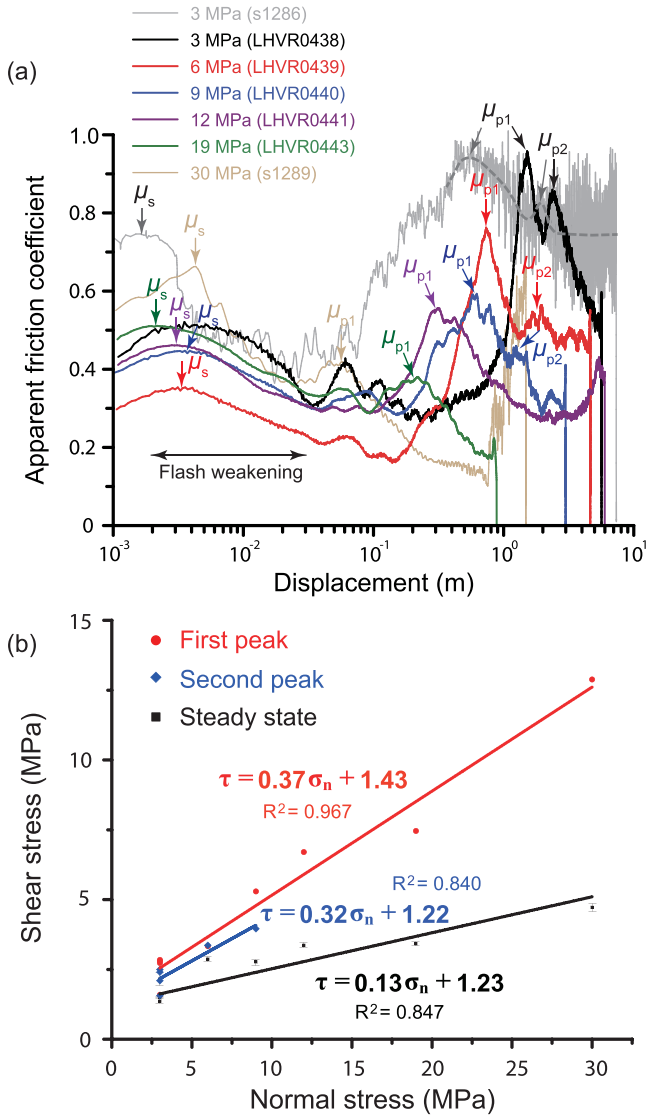

Figure 2. Mechanical and compiled data from experiments performed with LHVR and SHIVA machines. (a) Apparent friction coefficient as a function of displacement under normal stresses from 3 to 30 MPa and slip velocity at 1.3 m/s (LHVR) and 5 m/s (SHIVA) under room humidity (LHVR) and vacuum (SHIVA) conditions. The static friction, initial weakening, first peak, and second peak are indicated by the arrows. (b) Shear stress of the first peak (red circle), second peak (blue diamond), and steady-state value (black square) varied with normal stress. Note that the dynamic shear strength for peak states and steady state is well below Byerlee's friction values ($0.6 < \mu < 0.85$) (Byerlee, 1978).

minimum value (possibly associated with flash heating and weakening; see section 4). Then the frictional evolution varied with normal stress:

At large normal stresses (≥12 MPa; e.g., experiment s1289; Figure 2a) μ_{app} increased to a peak value μ_{p1} = 0.66 and then dramatically decreased to a low value of 0.16 ± 0.01 (an average value of friction coefficient after peak friction and before the sample was broken) defined in the literature as steady state friction μ_{ss} (e.g., Di Toro et al., 2011). At the end of slip, during sample deceleration, μ_{app} increased again. In general, this frictional evolution with slip is consistent with previous experiments performed on silicate-built cohesive rocks sheared at seismic slip rates (Di Toro et al., 2006; Di Toro, Hirose, Nielsen, Pennacchioni, & Shimamoto, 2006; Niemeijer et al., 2011; Passelègue et al., 2016; Shimamoto, 2005).

At low normal stresses (<12 MPa; e.g., experiments LHVR 0438 and LHVR0452; Figures 2a and 3), after slip initiation and initial flash weakening, μ_{app} first increased to a peak value at μ_{p1}~1.0, then decreased to 0.8–0.5, then increased again to a second peak value at μ_{p2}~0.44–0.83, and eventually decreased with displacement to μ_{ss}~0.3 ± 0.01–0.45 ± 0.08. Then, similarly to the large normal stress experiments, μ_{app} increased again at the end of slip (Figure 2a). This complicated evolution, though observed in previous experiments, has been only partly discussed (e.g., Shimamoto, 2005; Di Toro Hirose, Nielsen, Pennacchioni, et al., 2006).

With the aim of investigating the process responsible for the μ_{p1} and μ_{p2}, we analyzed the slipping zone produced in dedicated experiments stopped, with increasing slip (slip-stepping experiments; Figure 3), after (1) 1.5 m of slip corresponding to μ_{p1} (State A, experiment LHVR0487), (2) 2.6 m of slip corresponding to the frictional strength decrease between μ_{p1} and μ_{p2} (State B, experiment LHVR0534), (3) 2.1 m of slip corresponding to approximately μ_{p2} (State C, experiment LHVR0452), and (4) 5.7 m of slip during the final weakening (State D, "steady-state" conditions, experiment LHVR0438).

To illustrate the temperature evolution with slip for loading conditions identical to those imposed in the reference experiment LHVR0438 where steady-state conditions were achieved, experiment LHVR1097 was equipped with an infrared thermal-sensing camera. Because the emissivity ε of melt varies with temperature, we set two values of ε, 0.55 and 0.9 for high and low temperature, respectively (Abtahi et al., 2002). For ε = 0.55, the temperature of the slipping zone immediately increased to ~430 °C (approximately 0.6 m of slip in Figure 3e), slightly rose to ~500 °C at State A (approximately 1.2 m of slip), slightly decreased and remained a constant value of ~450 °C during State B (between 1.2 and 2 m of slip), steadily rose to ~750 °C at State C (between 2 and 3 m of slip), and eventually increased to a constant value of ~850 °C during State D (from 3 m to the end of slip). There was a loss of temperature measurements (between ~3.5 and 4 m of slip) because of connection issues with the infrared camera. For ε = 0.9, with respect to the estimated temperatures for ε = 0.55, temperatures achieved in the different States were lower by about ~100 °C for States A and B, ~200°C for State C, and ~250°C for State D.

Regarding the entire experimental data set, the initial peak (corresponding to μ_{p1}) and steady-state (corresponding to μ_{ss}) shear stress increased linearly with normal stress, resulting in an effective friction coefficient of ~0.3 and ~0.11 for μ_{p1} and μ_{ss}, respectively (Figure 2b). Instead, the second μ_{p2} disappeared with increasing normal stress (Figure 2a).

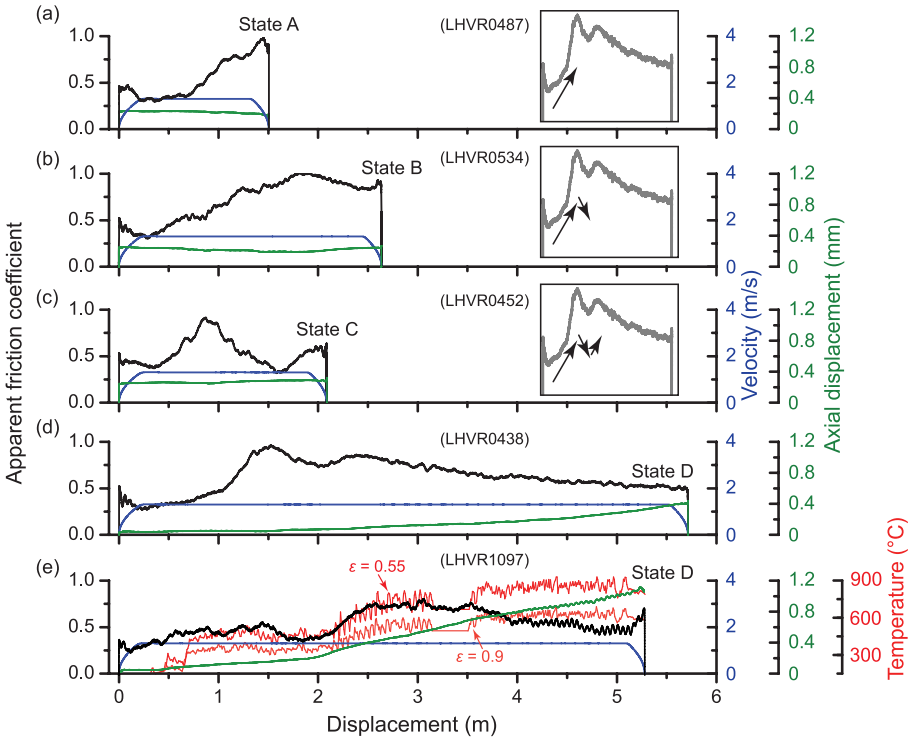

Figure 3. Evolution of the apparent friction coefficient, slip velocity, axial displacement, and temperature with displacement of five slip-stepping experiments. (a) State A (LHVR0487) stopped at the peak value representing the first slip-strengthening behavior. (b) State B (LHVR0534) was stopped at the second slip-weakening behavior. (c) State C (LHVR0452) stopped at the second slip-strengthening behavior. (d) State D (LHVR0438) was stopped at the steady-state value. (e) The experiment reproducing the condition of LHVR0438 with outcrop sample coupled with the infrared thermal-sensing camera. The temperature increases with slip from 150 °C (minimum detected value of the infrared camera) at the slip of ~0.4 m to ~850 °C ($\varepsilon = 0.55$) and ~600 °C ($\varepsilon = 0.9$) at the slip of ~5.3 m.

3.2. Microstructures, Mineralogy, and Chemical Composition of the Solidified Frictional Melt

We recovered the experimental products of the slip-stepping experiments and investigated with OM, FESEM-EDX, synchrotron XRD, and synchrotron TXM. The mineralogy and microstructures of the slipping zones are shown in Figures 4–6. In general, the thickness of the experimental slipping zones increases from the edge (were the slip rate is the highest) to the center (were the slip rate is nominally zero) of the circular slip surface (Figures 4a–4d). In the experiment stopped at State A, the solidified melt patches were discontinuous and meniscus-shaped (Figure 4). In the experiments stopped at States B and C, the solidified melt formed a continuous and dark-colored donut-shaped feature. In the experiment stopped at State D, the solidified melt covered the entire slip surface (Figure 4). In addition, the boundary solidified melt/host rock was irregular (presence of embayments, indicated by arrows in Figures 4a–4d) due to selective melting of the low-melting-point minerals (e.g., muscovite) of the granitic gneiss (see Hirose & Shimamoto, 2003; Figure 4d). The average thickness of the solidified frictional melt layers was determined by averaging the value of the real melt thickness obtained at different horizontal positions of the solidified melt on the slip surface. Although this measurement might result in an underestimate value as it includes the extrusion of melt at the end of slip, the melt thickness still notably varied at each state from ~270 μm in State A, ~330 μm in State B, ~170 μm in State C, and ~230 μm in State D (Table 2).

The in situ synchrotron XRD data show that the mineral assemblage of the host rock (black line) was composed of quartz, feldspar, calcite, and muscovite (Figure 4e). Instead, the clasts suspended in the solidified frictional melts produced in the slip-stepping experiments were mainly composed of quartz and minor feldspar (Figure 4e). As observed in both natural and experimental pseudotachylytes, this indicates that quartz is more resistant than feldspar and muscovite during comminution and melting (see Spray, 2010, for a review).

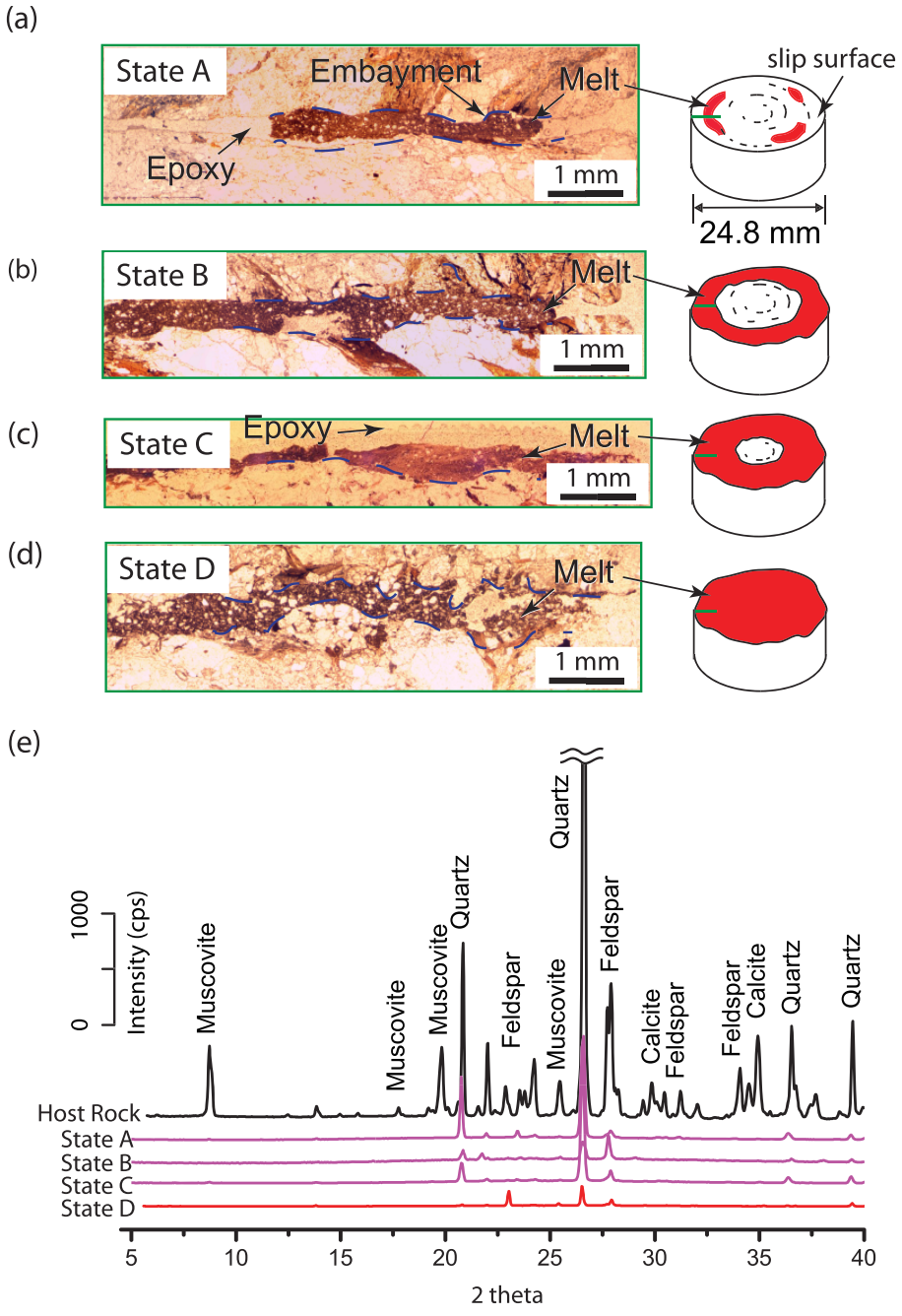

Figure 4. Experimental results of four states with corresponding schematic sketch of the solidified frictional melt distribution on the slip surface. The petrographic sections were prepared to be perpendicular to the slip surface and analyzed from half-way from the center to the edge. (a–d) Open Nicol observation of the experimental products. The frictional melt distribution evolves from the melt patches in State A, to a donut-shape melt layer in State B (5X intensity for compare) and C, to a fully covered melt layer in State D, respectively. (e) In situ synchrotron XRD analysis of the host rock and the experimental products from the simulated fault surface. The disappearance of the diffraction peak of mica and reduction of the diffraction intensity of feldspar and quartz are reflected in the XRD spectra and show no variation between the four states. The different colors between the melt spectra are indicated by the calculated bulk temperature where the red line refers to a higher melting temperature than the pink lines.

Unfortunately, the signals of the presence of amorphous materials (= glass matrix of the pseudotachylytes) between 15° and 40° of 2θ were not detected in the synchrotron XRD spectra because of the strong signal depression due to the high peaks of quartz.

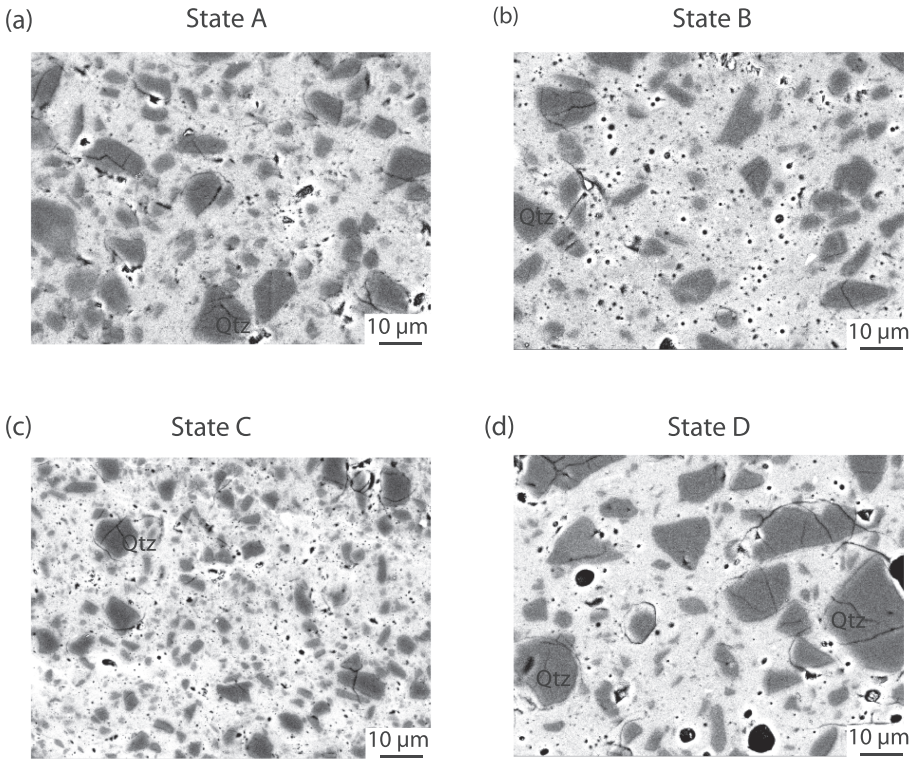

Figure 5. BSE images of the frictional melts for four states. (a) In State A, quartz grains (dark gray) with sizes ranging from 2 to 10 μm are abundant within the melt matrix (light gray). For (b), State B, the number of quartz grains with a size lower than 5 μm decreased. For (c), State C, smaller quartz grains (<1 μm) appeared while larger quartz grains (>10 μm) disappeared. For (d), State D, quartz grains with sizes larger than 10 μm are dominant within the melt. The dark area with spherical to ellipsoidal occurrence are vesicles, which are particularly larger in State D.

Under the FESEM-BSE, the grains of the undeformed Hoping granitic gneiss are angular and elongated in shape, with grain size varying from ~0.1 to ~1.0 mm (not shown). The representative BSE images of the solidified melts under identical magnification show a substantial amount of subangular quartz grains and the presence of vesicles distributed within the glass matrix (Figure 5). It is clear that the grain size distribution of the survivor grains of quartz varies significantly over the four states of the slip-stepping experiments; that is, grains <5 μm in size in State C are more abundant than in both States B and D (Figure 5 and section 3.5).

The TXM images show the overlapping of rounded to subrounded survivor grains which ranged from 50 nm to 10 μm in diameter within the solidified melts representative of the four states of the slip-stepping experiments (Figure 6). For grains <5 μm (size range that is difficult to be clearly observed under SEM-BSE), we find that the shapes of the survivor grains in the TXM images were in rounded or spherical shape, similar occurrence to the survivor quartz grains reported from Kuo et al. (2015). These results suggest that partial melting on the edge of grains likely occurred, in particular, for ultrafine grains (Kuo et al., 2015).

We utilized FESEM/EDS to analyze the matrix of the solidified frictional melts and adopted the average value of 40 points as representative of the chemical composition of the matrix (Table 1). The analysis showed no significant chemical variation of the composition of the solidified frictional melts from any of the four states of the slip-stepping experiments, except for the enrichment in SiO_2-content from State A to State C and particular high CaO content in State D. The Raman spectra of the slip-stepping experiments showed negligible water content in the solidified frictional melts (Figure 7).

3.3. Frictional Melt Viscosity and Temperature Estimate

In addition to the measured temperature of the frictional melt during the experiment LHVR1097, we also estimated the possible viscosity and temperature of the friction melt in the four states following the method suggested by Wallace et al. (2019). The non-Arrhenian Newtonian temperature-dependence viscosity of the

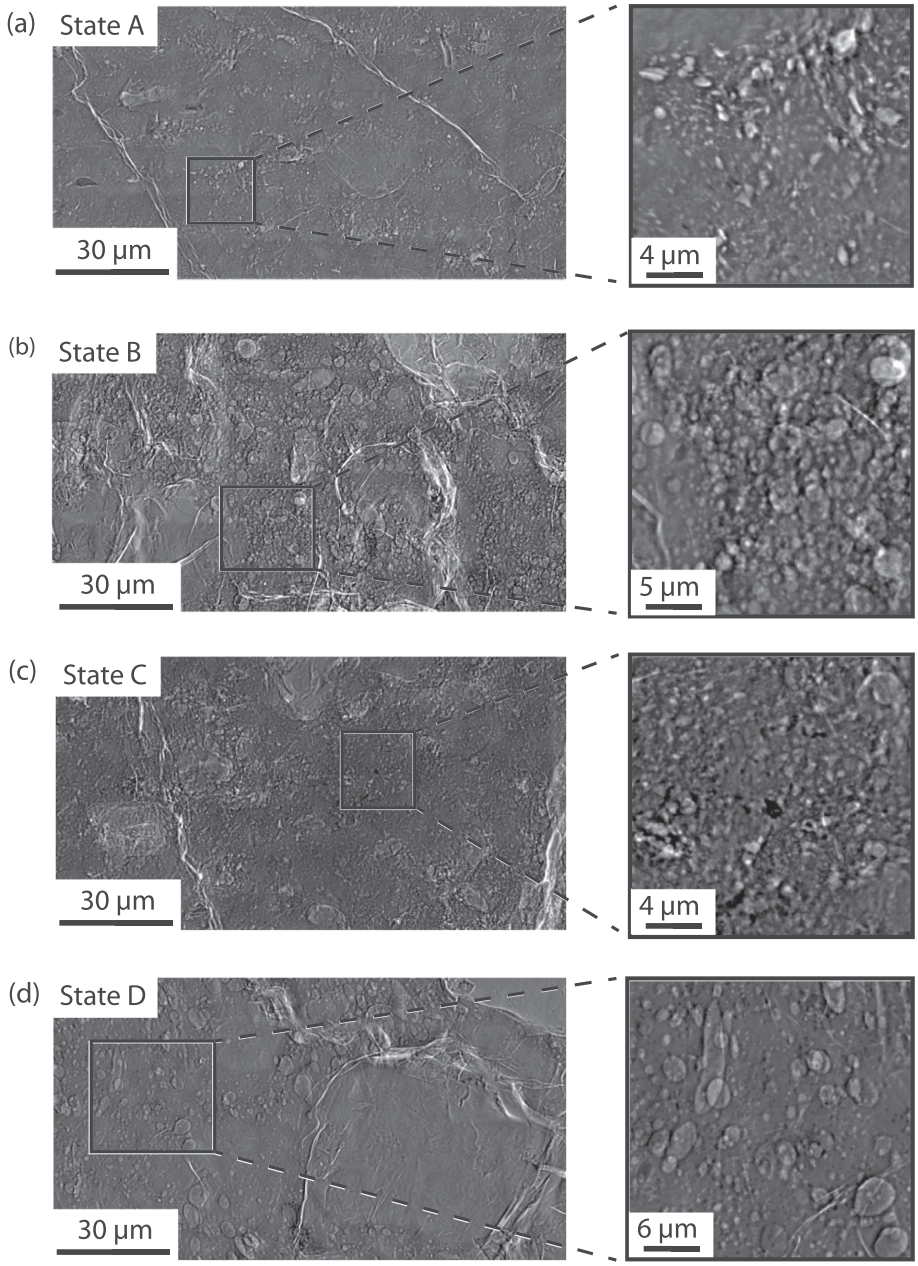

Figure 6. TXM images of the solidified frictional melts for the four states. Internal microstructures all show substantial ultrafine quartz grains with subangular and angular-to-spherical, and ellipsoidal surrounded by a melt matrix. (a) The enlarged image highlights the appearance of the fractured grains. (b) The enlarged image highlights the overlapping occurrence of ultrafine spherical quartz. (c) The enlarged image shows no distinct boundary of ultrafine quartz with a subangular to the spherical shape. (d) The enlarged image shows a distinct occurrence of ultrafine spherical to ellipsoidal quartz.

silicate melt can be estimated by the GRD viscosity calculator (available online at https://www.eoas.ubc.ca/~krussell/VISCOSITY/grdViscosity.html) by inputting the melt composition (Table 1; Giordano et al., 2008; Lavallée et al., 2012). This calculation is based on the Vogel-Fulcher-Tamman equation:

$$\mathrm{Log}\,\eta = \mathrm{A} + \frac{B}{T(K) - C} \tag{5}$$

where the η is viscosity (Pa s); A, B, and C are the modeled parameters based on viscosity measurement of geochemical composition (Giordano et al., 2008); and T is the silicate melt temperature (K). We obtained the

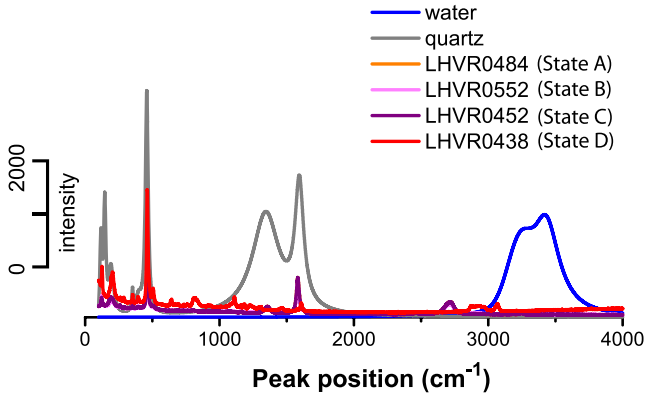

Figure 7. Representative Raman spectra of the glass from four states, quartz, and water. The signal for the presence of water is barely observed for each state.

viscosity curves for the slip-stepping frictional melts (Figure 8) by giving at the constant A the value of −4.55 (optimal value based on Giordano et al. (2008)), and the values of B and C were obtained from the chemical composition of the glasses and 17 adjustable parameters (see demonstration calculation in Giordano et al. (2008); Table 1). The presence of vesicles suggests that some volatiles (e.g., OH from muscovite) were present in the melt, but the water content in the glass was likely negligible and assumed to be zero based on the absence of water signal from Raman analysis (Figure 7).

Based on the mechanical data, the apparent viscosity of the frictional melts (η_{app}) can be directly calculated by the ratio of the measured shear stress to the strain rate as

$$\eta_{app} = \frac{\tau}{\dot{\varepsilon}} = \frac{\tau w}{V_e}\ [Pa\ s] \tag{6}$$

where τ is the measured shear stress (Pa), $\dot{\varepsilon}$ is the strain rate (s^{-1}), w is the thickness of the melt layer (an underestimate of the thickness during sliding as it includes the extrusion of melt at the end of slip), and V_e is the equivalent slip velocity (m/s). Because solid particles (= survivor clasts) are present in the frictional melts, the calculated apparent viscosity could be overestimated (e.g., Metzner, 1985). To correct the effect of clasts on the apparent viscosity, we calculated the relative viscosity (η_r) using an empirical equation (Kitano et al., 1981):

$$\eta_r = \left(1 - \frac{\phi}{A}\right)^{-2} \tag{7}$$

with $A = 0.54–0.0125r$, where ϕ is the volume fraction (volume particles/total volume) of the clasts, A is the parameter related to the packing geometry of the solid particles, and r is the average aspect ratio of solid

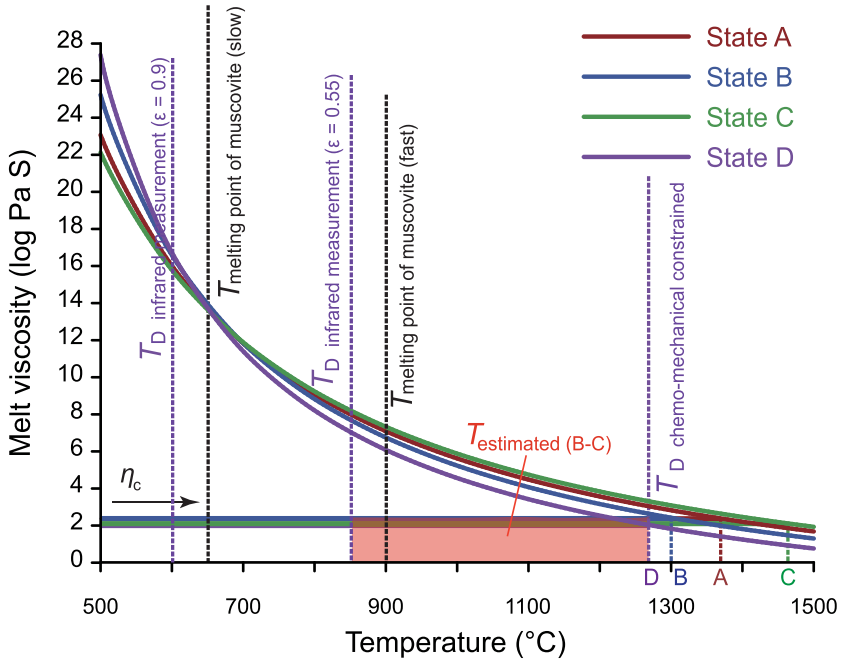

Figure 8. Non-Arrhenian temperature dependence of viscosity for four states. The viscosity curves were derived using the GRD viscosity model of the Giordano et al. (2008) based on the chemical composition of the glass matrix. The apparent viscosity corrected with clast content (η_c) was derived from the mechanical data. Intersection points are the estimates of temperature of chemo-mechanical data for the four states. The temperatures achieved for states A to C were estimated between the achieved temperature of State D and the melting point of muscovite obtained by slow heating (650 °C) and fast heating rate (900 °C) experiments. See the main text for further discussion. Two temperatures obtained by infrared measurement from emissivity (ε) of 0.55 and 0.9 were plotted.

grains (about 2 in our case). We measured the ϕ using BSE images from the center to the edge of the experimental pseudotachylyte and averaged the value. The value of ϕ ranged from ~0.11 at State C to ~0.20 at States A, B, and D (Table 2). Moreover, the presence of vesicles should lower the apparent viscosity of the frictional melt (e.g., Manga et al., 1998). However, the volume fraction of the vesicles is small (<0.1) and shows no significant variation in the four states. Therefore, the contribution of the vesicles to the apparent viscosity should be negligible (Lejeune et al., 1999). Based on equations (6) and (7), the mechanically constraint apparent viscosities corrected with the presence of clasts ($\eta_c = \eta_{app}/\eta_r$) are ~229 Pa s at State A, ~232 Pa s at State B, ~125 Pa s at State C, and ~99 Pa s at State D (Table 2).

According to the model for non-Arrhenian temperature dependence of melt viscosity (equation (5); Wallace et al., 2019), the chemically and mechanically constraint apparent viscosities for the four states are consistent with the temperature of ~1,370 °C (State A), ~1,300 °C (State B), ~1,456 °C (State C), and ~1,265 °C (State D; Figure 8). These chemo-mechanical-constraint temperature estimates are at odds with the temperature measured estimated with the infrared camera, as it will be discussed in section 4.3.

3.4. Particle Size Distribution (PSD)

The PSD was obtained by measuring all clasts (mainly made of quartz) within the solidified frictional melt from the images of both SEM and TXM. With the FESEM, for each state, we collected 8 to 12 BSE contiguous images to cover almost entirely slipping zone. Moreover, we collected some images at higher magnification (1,300X; similar to Figure 5) to obtain more accurate size distribution on finer grains (<10 μm). With the TXM, for each state, we analyzed identical areas of 375 μm in length and 75 μm in width, corresponding to the central part of the slipping zone. Since the TXM images included all the grains over the entire thickness (30 μm) of the thin section, the number of particles measured from the TXM images has different unit compared to that from BSE images (i.e., number of particles per μm^2 for SEM and per μm^3 for TXM). Therefore, we further divided the obtained data from the TXM images by the sample thickness (μm) to integrate it with the PSD data from the BSE images. To increase the accuracy of the density data in size range of 1–3 μm (lower limit of SEM analysis), we extend the TXM results to overlap this size range. The density data in this overlapping range are reported as the average value of both TXM and SEM results.

The PSD data were plotted as a cumulative frequency diagram for the mean diameter, r, using a logarithmic scale. Our results (solid dots) were fitted and plotted with solid curves for mean diameters >1 μm and as dashed lines for diameters <1 μm. The particle density, $N(r)$, which represents the cumulative number of particles per μm^2, follows a function of mean diameter (r), defined as the geometric mean of the major and minor axes of an irregular grain, in the form of a power law for frictional melting (not comminution): $N(r) = N'(1 + r/r')^{-D}$, where N is the cumulative number of grain sizes greater than r, that is, N' (which depends on the total number of measurements), r' is constant, and D is the fractal dimension (Shimamoto & Nagahama, 1992; Tsutsumi, 1999).

The fitted curves for each state are almost identical; that is, the curves are steep in the coarse-grained size ranges (>10 μm) and gently flatten toward fine size <10 μm, and to some degree the PSDs obey to a power law (Figure 9). Interestingly, we find that the measured particle density for the grain sizes smaller than 1 μm is larger than the fitted curves, in particular, at States A and B (Figure 9). Based on the previous PSD studies of the experimentally produced pseudotachylytes, the slope of the PSD curves shows a linearly steep to horizontal evolution in the size range from about 100 to 0.5 μm (e.g., Tsutsumi, 1999; Figure 2). These curves were obtained from the solidified melt with long displacement experiments (hundreds of meters) and the change of the slope was suggested to be the effect of partial melting of the survivor grains. Therefore, compared to our results obtained from the short-displacement experimental melt (<3 m), the deviation between measured density data and fitted curves in size <1 μm, particularly significant in States A and B, may suggest that the ultrafine quartz grains derived from the surface comminution are trapped in the melts. Instead, the PSD of the clasts from State C is described by a larger value for D. The reduced thickness of the slipping zone during frictional melting is one of the factors controlling the size reduction of the clasts in the coarse-grained range and, as a consequence, the fractal dimension of their distribution (Tsutsumi, 1999). In addition, thickness of the melt zone might strongly depend on the viscosity and thus on the temperature of the melt layer. This may suggest that the high value of D at State C might be controlled by the melt thickness (the thinnest among the slip-stepping experiments). But here we cannot evaluate how the size reduction and melt viscosity influence the D value due to their complicated correlation and more comprehensive studies are required.

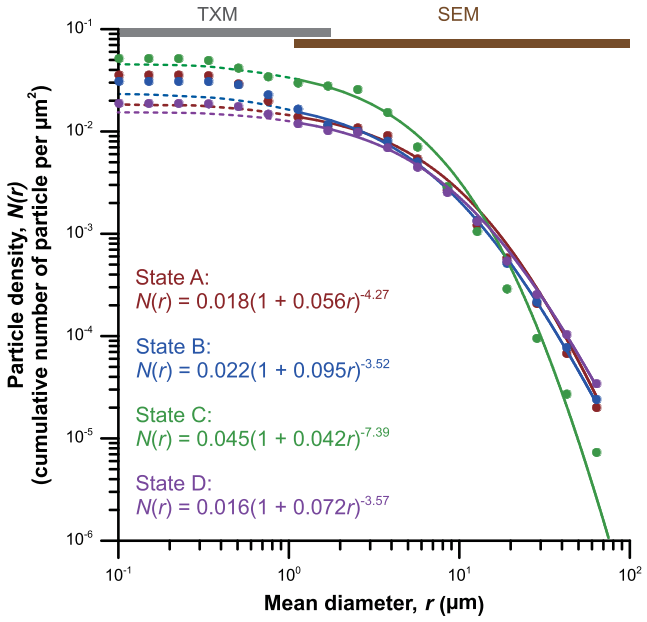

Figure 9. Particle size distribution of surviving grains within the melt matrix for four states. Cumulative particle density as a function of mean diameter. The particle density, $N(r)$ representing the cumulative number of particles per μm^2, following a function of particle mean diameter (r) in micrometers with regression lines (solid lines) in a form of power law $N(r) = N'(1 + r/r')^{-D}$. The obtained particle density from TXM analyses is relatively higher than the interpolated regression line (dashed line) for the four states.

4. Discussion

4.1. Frictional Evolution During Fast Fault Slip at Low Normal Stress

We focus on the complicated frictional evolution of granitic melts at low normal stress. Chen et al. (2017b) performed frictional experiments on granitic rocks for moderate velocities (0.01–0.11 m/s) to investigate the complicated frictional evolution with slip at the transition between powder lubrication and melt lubrication. They suggested that the evolution of the frictional behavior can be divided into three stages based on different physical mechanisms: the initial weakening stage (Stage 1: powder lubrication), the initial strengthening stage (Stage 2: viscous melt patches), and the final weakening stage (Stage 3: melt lubrication; Figure 10a). They concluded that this complicated frictional evolution is the result of thermally activated deformation processes. In the discussion below, we exploit the conceptual model proposed by Chen, Madden, and Reches (2017b) to our experimental data set. At slip initiation, during Stage 1, we propose that flash heating and melting of the asperity contacts is the dominant weakening mechanism once a threshold sliding velocity of >0.1 m/s (case for silicate-built rocks) is achieved (Rice, 2006; Di Toro, Hirose, Nielsen, & Shimamoto, 2006; Shimamoto, 2005; Niemeijer et al., 2011; Goldsby & Tullis, 2011; Proctor et al., 2014; Violay et al., 2014; Figures 10b–10e). Then, we divide the Stage 2 of Chen, Madden, and Reches (2017b) (dynamic fault strengthening in the presence of powders and melt patches) into States A (first peak), B, and C (second peak) and keep Stage 3 of Chen, Madden, & Reches, 2017b (weakening due to the presence of a continuous melt layer) as our State D (see also discussion in Shimamoto, 2005; Di Toro, Hirose, Nielsen, & Shimamoto, 2006; Niemeijer et al., 2011; Violay et al., 2014; Proctor et al., 2014; Figures 10b–10e). Below we focus on the complex frictional evolution during Stage 2.

4.2. Initial Strengthening in Stage 2 (State A)

At slip initiation, when flash heating occurs, temperatures significantly rise at the asperity scale and melt the rock contacts (Rice, 2006). In addition, rubbing of the asperity contacts induces tribo-chemical reactions and triggers different mechanisms. Therefore, tribo-chemical reactions may occur at lower activation energies (and thus their kinetics is more efficient at a given temperature) than thermo-chemical reactions (Steinike & Tkáčová, 2000). It is reasonable to assume that flash heating of the granitic gneiss may result in the preferential fusion of the low melting point minerals (i.e., muscovite, T_m = 650 °C–900 °C at 1 atm; Spray, 2010, see discussion below) but also in the formation of silica-rich melt droplets from fusion of high melting point minerals as quartz (main mineral of the gneiss, T_m = 1,720 °C at 1 atm; Spray, 2010). The melt patches in State A were derived from the accumulation of the melt droplets produced by flash heating and melting at the asperity contacts, resulting in the formation of relatively silica-rich melts.

In addition, the PSD data of State A show the presence of ultrafine grains, suggesting an additional source of grains into the melt. When frictional melts occurred and covered the entire slip surface, the survivor grains were mainly derived from thermal cracking and frictional melting of the wall rocks and sticking out from the wall rocks into the melt. Based on this, compared to the PSD of State D, we conclude that the additive grains in State A were the result of mixtures of rock clasts (by rock fragmentation) and melt patches during initial sliding.

The temperature measured with the infrared camera at State A is ~500 °C, and it is likely an underestimated because of (1) averaging with the slipping zone and the wall-rocks and (2) slightly unfocused measuring (outside of the slipping zone). Integrated with the mineralogical observation (Figure 4e), the temperature at State A should achieve the breakdown point of muscovite (at least >650 °C) and was relatively lower than the other states (with shorter slip and less frictional work input; see the details in section 4.3). Therefore, the estimated temperature and corresponding viscosity (Figure 8 and Table 1) indicate that the silica-rich melt

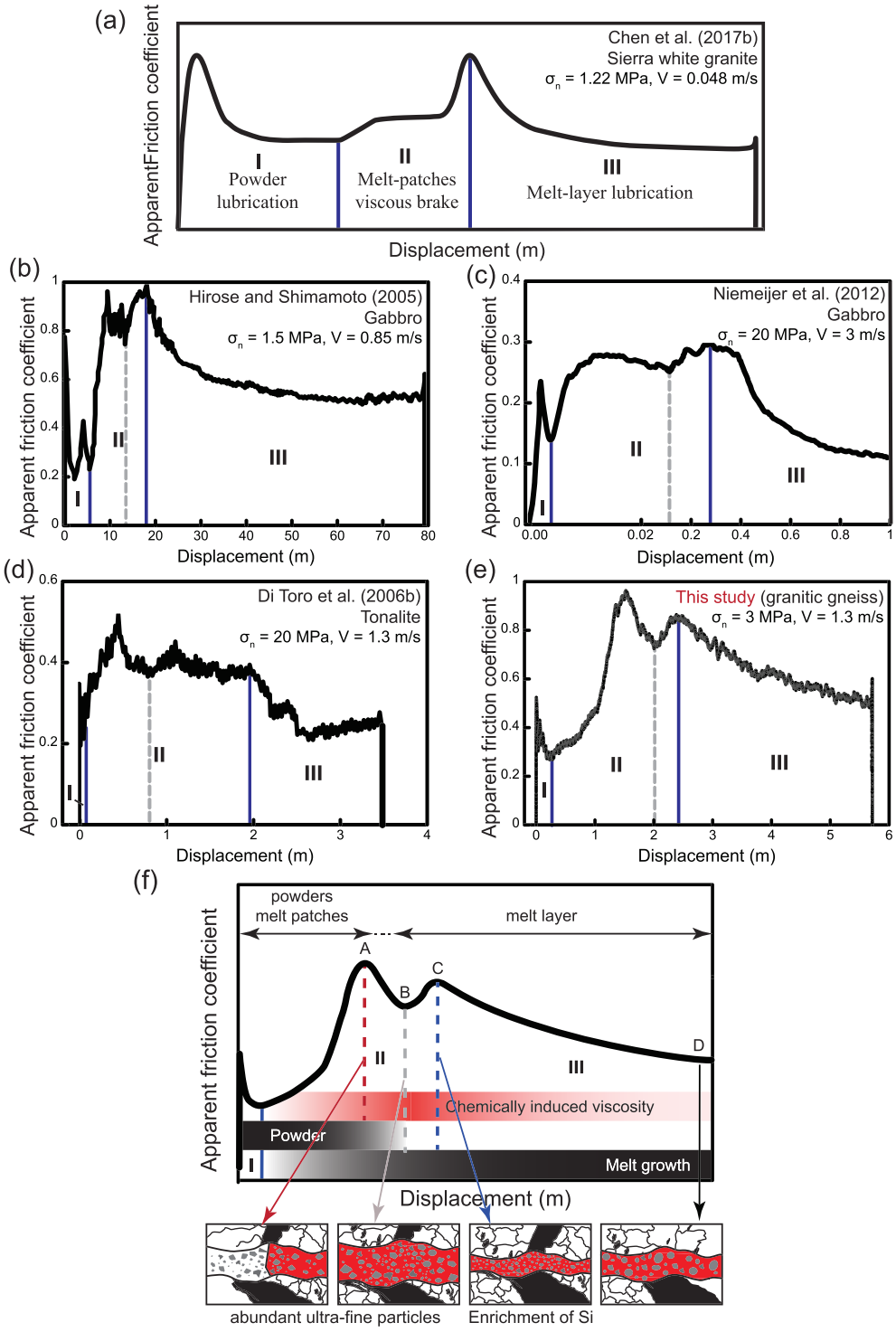

Figure 10. Frictional evolution with displacement for crystalline silicate rocks. (a) Schematic sketch of the frictional evolution of Sierra white granite sheared at a slip velocity of 0.048 m/s under a normal stress of 1.22 MPa (after Chen, Madden, & Reches, 2017b). The associated slipping mechanisms corresponding to each stage were shown. (b) Indian Gabbro sheared at a slip velocity of 0.85 m/s under a normal stress of 1.5 MPa (after Shimamoto, 2005). (c) South Africa gabbro sheared at a slip velocity of 3 m/s under a normal stress of 20 MPa (after Niemeijer et al., 2012). (d) Tonalite sheared at a slip velocity of 1.3 m/s under a normal stress of 20 MPa (after Di Toro, Hirose, Nielsen, & Shimamoto, 2006). (e) Schematic sketch of the frictional evolution of granitic gneiss sheared at a slip velocity of 1.3 m/s under a normal stress of 3 MPa. Similar to Chen, Madden, and Reches (2017a), the evolution of powder, melt growth, and temperature with displacement is further added into our conceptual model and Stage 2 is further delimited into two regimes by the gray line. The four schematic diagrams of the slipping zone summarize how the PSD, particle volume fraction, melt distribution, microstructures, and clast packing varied with frictional evolution with slip for the reference experiment LHVR0438.

patches of State A were highly viscous and presumably contributed to the resistance of shearing, resulting in the initial strengthening in Stage 2, similar to the observation reported by Chen, Madden, and Reches (2017b).

4.3. Restrengthening in Stage 2 (States B to C)

With progressive sliding, the melt patches accumulated into a donut-shaped melt layer and the two rock specimen were partly separated from the melt layer (States A to B; Figure 4b). Here we simply neglect the contribution from solid-solid friction in the central part of the slip surface because the torque and thus the shear stress increase with sample radius (e.g., equation (2)), where the frictional contribution from the inner part of the cylinder is negligible (Shimamoto, 2005). In addition, because the microstructural observation shows that solidified melts were thicker than the surface roughness (Figure 4), the solid-solid contacts at the outer melt regime were unlikely to have occurred. We suggest that donut-shaped melt layer is the main contribution for shear resistance during the experiment. As a consequence, melt viscosity and shear strain rate are the dominant parameters that control the shear resistance of the simulated fault during the frictional melting regime (States B to D).

Melt viscosity is controlled by three parameters: temperature, presence of water, and chemical composition (Lejeune et al., 1999; Fluegel et al., 2004). According to the mechanically constraint viscosity model (section 3.3), the temperatures achieved in States A to D are about 1,370 °C, 1,300 °C, 1,456 °C, and 1,265 °C, respectively (Figure 8). The estimated temperature of State D (melt lubrication regime) is in good agreement with previous rock friction experiments conducted at seismic slip rates (Shimamoto, 2005; Di Toro Hirose, Nielsen, Pennacchioni, et al., 2006; Niemeijer et al., 2011, 2012; Nielsen et al., 2008). The estimated temperature of State D (1,265 °C) can be set as the upper bound for the temperature achieved in the slip-stepping experiments. In fact, the temperature achieved in States A to C should be lower than the one achieved during State D because, under the same conditions, the shorter slip also imply less work input by the motor. Therefore, according to the evaluation of temperature at State D, the estimated temperature of State C (1,456 °C) is overestimated.

On the basis of the mineralogy of the survivor clasts (e.g., muscovite was melted through all the slip-stepping experiments; Figure 4e), we can take the melting point of muscovite into consideration to estimate the temperature of the friction melt. The melting point (T_m) of muscovite during static heating at a low heating rate of 1 °C/min is 650 °C (Spray, 2010) and T_m increases to 900 °C at a high heating rate of 200 °C/min (Kuo et al., 2011). Because of the difficulty of evaluating on one side the contribution of grinding processes during frictional sliding that may further lower the T_m of muscovite and, on the other side the heating rate which is much higher than the aforementioned heating rates tested in the laboratory (e.g., Kuo et al., 2011), we assume that the lower bound of the temperature achieved during States B and C is ~900 °C.

In experiment LHVR1097 we measured the temperature evolution from States A to D (Figure 3e). The temperature measured by the infrared camera is affected by (1) absorption (i) of emitted radiance by gases produced during frictional sliding (SO_2, H_2O, CO_2) and (ii) of the powders suspended in the air, (2) variance of emissivity (ε), and (3) the thickness of the slipping zone which is thinner than the area investigated by the infrared camera (i.e., the camera measures the temperature over an area that includes both the hot slipping zone and the cold wall rocks). As a consequence, the temperature measured with the infrared camera is commonly considered as an underestimated value. Abtahi et al. (2002) reported that broadband emissivity systematically rises as the lava cools, from 0.55 at 1,050 °C to 0.85 at <500 °C. In our case, the widespread preferential melting of muscovite demonstrates that temperatures were higher than 650 °C in the slipping zones of States A to D. As a consequence, it seems that a low value of emissivity ($\varepsilon = 0.55$) is more appropriate for the temperature measurements with the infrared camera, and thus, the associated estimated temperature is ~850 °C, as the lower bound of temperature of States B and C. Taken together, the achieved temperatures for States A to C should be in the range of 850 °C to 1,265 °C (the pink area in Figure 8).

In the temperature range of 850 °C to 1,265 °C, the viscosity of the melt in State C is higher than the one achieved in the other states ($10^{8.0}$–$10^{3.1}$ Pa s, $10^{7.7}$ –$10^{2.7}$ Pa s, $10^{8.2}$–$10^{3.3}$ Pa s for States A to C, respectively). In addition, the slope of the non-Arrhenian temperature dependence of the viscosity curves become less steep. This suggests that even if the temperature of the melt increases with slip between States B and C

(i.e., temperature at State C is slightly higher than the one at State B; Figure 3e), the estimated viscosity at State C can be higher than the one at State B.

To summarize, because of frictional heating, the bulk temperature in the slipping zone increases with slip (Figure 3e) and likely reduces the melt viscosity, resulting in melt lubrication (Di Toro Hirose, Nielsen, Pennacchioni, et al., 2006). However, by itself, the gradual temperature increase, which would result in less viscous friction melts, is at odds with the re-strengthening behavior (i.e., μ_{p2} occurred at an higher temperature than μ_{p1}; Figures 2 and 3e). On the basis of the temperature-viscosity model (Figure 8), the evolution of the chemical composition of the frictional melt with slip might be the most plausible explanation for re-strengthening from States B to C. Although water was present at the initiation of slip (the experiments were performed under room-humidity conditions) and released by the breakdown of muscovite, because of the not-confined conditions, gases could escape from the frictional melt. This resulted in the formation of vesicles and in the negligible water content of the pseudotachylyte matrix (Raman spectroscopy data in Figure 7). As a consequence, water cannot be responsible for the variation of the viscosity of the melt in any of the States. On the other hand, the experiment s1286 under vacuum conditions (Table 1) may further indicate the re-strengthening is irrelevant to the humidity and/or oxidation. Taken together, the increase in SiO_2 in the frictional melt might be the most plausible contributor for the re-strengthening from State B to State C (Table 1).

The presence of clasts made of quartz and, to a less extent, feldspar and the absence of muscovite in the solidified frictional melt (Figures 4e and 5) suggest that selective melting of low-melting-point minerals (i.e., muscovite) took place (Shand, 1916; Sibson, 1975; Spray, 1987). However, the chemical composition of the glass matrix at States B and C is higher in SiO_2 and lower in CaO (Table 1) compared to the composition of the glass matrix at State D which was produced at higher temperatures (Figure 3e). This chemical variation suggests that partial melting of quartz was more efficient at States B and C than State D while partial melting of feldspar was comparatively efficient at State D. In fact, during State D the sliding surfaces were entirely separated by the frictional melt (Figure 4d) and grain fragmentation due to solid-solid contact of the asperities was less efficient than during States A to C. Therefore, the presence of rock powders (mostly made by quartz and feldspar) in the frictional melts likely drove further melting of the small grains by quasi-equilibrium melting (Lee et al., 2017) or by the Gibbs-Thomson effect due to the high surface-to-area ratio (Hirose & Shimamoto, 2003). These particular melting processes resulted in the increase of Ca (although not obvious in our result) and especially Si content in the frictional melt and, as a consequence, in the increase of the melt viscosity from State B to State C (Table 1). Without the addition of fragmentation products, the chemical composition of the glass matrix at State D was then mainly derived from the melting of feldspar and muscovite.

We propose that the enrichment in Si in the frictional melt associated to grain-by-grain fragmentation at the initiation of simulated seismic slip may explain the observed fault re-strengthening observed in previous experiments performed at seismic rates (Di Toro, Hirose, Nielsen, & Shimamoto, 2006; Shimamoto, 2005; Niemeijer et al., 2011; Figure 10). Moreover, this process of chemical evolution of melt composition with slip also support the model proposed by Fialko and Khazan (2005) according to which thermal-activated slip strengthening is likely to occur in quartz-rich rocks at shallow depths.

4.4. Final Weakening During Stage 3 (State C to D)

The final fault weakening is observed in all the experiments, but of course not in the short slip-stepping experiments (Figure 2b), and is associated to the formation of a continuous frictional melt layer (Figure 4d). In fact, frictional melts with high temperatures and low silica content (Table 1) are an efficient lubricant, consistently with previous experimental and theoretical studies (Di Toro, Hirose, Nielsen, Pennacchioni, & Shimamoto, 2006; Di Toro, Hirose, Nielsen, & Shimamoto, 2006; Nielsen et al., 2008; Niemeijer et al., 2011, 2012; Shimamoto, 2005). In addition, our mechanical data are comparable to those of previous experiments on tonalite (similar mineral assemblages without foliation) where both data show low effective friction coefficient (0.13 and 0.05, respectively) at the steady-state melting (Di Toro, Hirose, Nielsen, Pennacchioni, & Shimamoto, 2006; Di Toro, Hirose, Nielsen, & Shimamoto, 2006). This suggests that the mineralogical heterogeneity of the specimens due to the metamorphic foliation makes only a very minor influence on the obtained values of shear stress.

4.5. Rock Friction Experiments and Re-Strengthening Behavior

The mechanical data show a complicated evolution of the friction coefficient (flash weakening, first strengthening, slight weakening, second strengthening, and eventually weakening) with slip at low normal stresses (<10 MPa; Figure 2a). This complicated evolution almost disappears and approximates an exponential decay at larger normal stresses (e.g., 30 MPa; Figure 2a). The most significant change with increasing normal stress is the reduction of the first peak value μ_{p1} and the disappearance of the second peak μ_{p2} (Figure 2a). This is the result of the more continuous transition from flash weakening to melt lubrication with increasing normal stress, but also with increasing slip rate and slip acceleration rate (5 m/s and 6.5 m/s^2, respectively, for the experiments performed with SHIVA). In fact, the higher heat production rate, proportional to the product of the normal stress per slip rate, dissipated on the slipping zone results in the fast generation of the frictional melt and rapid reduction of the friction coefficient. Therefore, at larger normal stresses and slip rates, the effect of surface comminution becomes negligible during the onset of slip.

In the case of the experiments performed with SHIVA, sample preparation (pregrounding process) can influence the frictional evolution with slip. Niemeijer et al. (2011) pregrounded the samples with SHIVA to achieve perfect alignment and obtained a complicated friction evolution afterward. It seems that, by doing this, ultrafine powders were likely generated and potentially stuck on the asperities of the slip surface, even though the powder was cleaned with an air brush before the high-speed experiment. Nielsen et al. (2012) applied a new method to align the SHIVA samples without pregrinding the slip surfaces and obtained a simpler evolution (which approximated an exponential decay) of the friction coefficient at slip initiation (Violay, Di Toro, et al., 2014,Violay, Nielsen, et al., 2014; Violay et al., 2019). Therefore, both SHIVA and LHVR results demonstrate the presence of a correlation between the presence of fragments in the slipping zone and the second re-strengthening behavior.

4.6. Implications for Natural Hoping Pseudotachylyte

We apply our experimental results to the natural observations of the Hoping pseudotachylyte. Ferré et al. (2016) proposed to use a novel linear structure decorating the slip surfaces of pseudotachylytes, described as "brushlines," to identify the coseismic slip direction. The brushlines were suggested to form through viscous brushing between protruding asperities of the host rocks and the viscous frictional melt (solid-liquid interaction) during rapid cooling at the end of slip. The chemical compositions of the Hoping pseudotachylyte (average 61% silica content; Kuo, 2016) and of the experimental pseudotachylytes from the same rocks generated in State C (Table 1) are very similar. It implies that the Hoping pseudotachylyte likely formed during small seismic slip events or at the initial fault sliding (corresponding to State B to C) and contained remnant grains from fault comminution. If so, our finding about the chemically induced increased viscosity of the frictional melt might be another explanation for the process of viscous brushing.

5. Conclusions

In this study, we present the mechanical results of slip-stepping experiments performed on solid cylinders of granitic gneisses sheared at high slip velocities using rotary shear machines (SHIVA and LHVR) coupled with high-resolution microstructural (scanning electron microscope, transmission X-ray microscopy, image analysis, etc.) and mineralogical (synchrotron X-ray diffraction analysis, micro-Raman spectroscopy, etc.) investigations of the experimental fault products. In the case of the experiments performed at seismic slip rates (1.3 to 5 m/s) but low normal stress (<10 MPa), the mechanical data show a complicated frictional evolution with slip which includes initial weakening, first strengthening followed by a slight decrease, and then by a second strengthening and a final exponential decay toward a steady state value (Figures 2 and 3). This complex frictional evolution becomes less pronounced in the experiments performed at larger normal stresses and is associated with the evolution of the viscosity of the frictional melts (chemical composition, temperature, etc.; Figures 4–9 and Table 1). We thus modified the model of Chen, Madden, and Reches (2017b) for the various friction behaviors (stages 1 to 3) associated with different physical mechanisms (Figure 10). We propose that the initial fault weakening is due to the grain fragmentation and flash heating and weakening on bare rock surfaces. The first fault strengthening is due to braking from the formation of a highly viscous (also because of the low temperature) frictional melt. The second fault re-strengthening is associated with the increased viscosity mainly because of the SiO_2 enrichment of the frictional melt. The increase in SiO_2 content is probably due by a combination of quasi-equilibrium melting and the Gibbs-

Thomson effect on the ultrafine quartz grains. The final weakening is due to melt lubrication because of the formation of a continuous melt layer covering the entire slip surface together with the reduction of the viscosity because of the increased temperature of the melt.

Considering the experimental conditions at which the chemically induced high viscosity frictional melt forms, we suggest that the surging of frictional melts generated behind the rupture front likely hampers seismic slip during initial earthquake propagation at shallow depths, even though melt lubrication takes place afterward. As a natural example, although the Hoping pseudotachylytes were generated at depths >4 km, our result suggests that the chemically induced high viscosity frictional melt formed in the Hoping area may therefore play a braking role during fault rupture into shallow depths.

Acknowledgments
This research was supported by the European Research Council Consolidator Starting Grant 614705 NOFEAR to Giulio Di Toro and Taiwan ROC (Republic of China) Ministry of Science and Technology grant MOST 108-2116-M-008-021-MY2 to Li-Wei Kuo. Samples were prepared by Jialiang Si via the National Science Foundation of China (41572192, 41330211). We thank Taiwan Power Company and Industrial Technology Research Institute for providing the Hoping borehole cores, and Che-Ming Yang and Hsiu-Ching Hsiao for their laboratory support. The experimental data supporting this work are publicly available online (http://140.115.20.219:5000/sharing/VTj4nVZcU).

References

Abtahi, A. A., Kahle, A. B., Abbot, E. A., Gillespie, A. R., Sabol, D., Yamada, G., & Pieri, D. C. (2002). Emissivity changes in basalt cooling after eruption from Pu'u O'o [abs.]. *Eos, Transactions of the American Geophysical Union*, *83*.

Beeler, N., Tullis, T., & Goldsby, D. (2008). Constitutive relationships and physical basis of fault strength due to flash heating. *Journal of Geophysical Research*, *113*, B01401. https://doi.org/10.1029/2007JB004988

Brodsky, E. E., & Kanamori, H. (2001). Elastohydrodynamic lubrication of faults. *Journal of Geophysical Research*, *106*, 16,357–16,374. https://doi.org/10.1029/2001JB000430

Byerlee, J. (1978). Friction of rocks, Pure Appl. *Geophysica*, *116*, 615–626. https://doi.org/10.1007/BF00876528

Chen, C.-T., Wu, C.-Y., Lo, C.-H., Chu, H.-T., & Yui, T.-F. (2017). Dating palaeo-seismic faulting in the Taiwan Mountain Belt. *Terra Nova*, *30*(2). https://doi.org/10.1111/ter.12319

Chen, X., Madden, A. S. E., & Reches, Z. (2017a). Powder-rolling as a mechanism of dynamic fault weakening. In M. Thomas, T. Mitchell, & H. Bhat (Eds.), *Fault zone dynamic processes: Evolution of fault properties during seismic rupture*, (pp. 133–150). Washington, DC and Hoboken, NJ: American Geophysical Union and John Wiley. https://doi.org/10.1002/9781119156895.ch7

Chen, X., Madden, A. S. E., & Reches, Z. (2017b). Friction evolution of granitic faults: heating controlled transition from powder lubrication to frictional melt. *Journal of Geophysical Research: Solid Earth*, *122*, 9275–9289. https://doi.org/10.1002/2017JB014462

Chu, H.-T., Hwang, S.-L., Shen, P., & Yui, T.-F. (2012). Pseudotachylyte in the Tananao Metamorphic Complex, Taiwan: Occurrence and dynamic phase changes of fossil earthquakes. *Tectonophysics*, *581*, 62–75. https://doi.org/10.1016/j.tecto.2012.01.017

Collettini, C., Viti, C., Tesei, T., & Mollo, S. (2013). Thermal decomposition along natural faults during earthquakes. *Geology*, *41*, 923–930. https://doi.org/10.1130/G34421.1

Cornelio, C., Spagnuolo, E., Di Toro, G., Nielsen, S., & Violay, M. (2019). Mechanical behavior of fluid-lubricated faults. *Nature Communications*, *10*(1), 1274. https://doi.org/10.1038/s41467-019-09293-9

De Paola, N., Holdsworth, R. E., Viti, C., Collettini, C., & Bullock, R. (2015). Can grain size sensitive flow lubricate faults during the initial stages of earthquake propagation? *Earth and Planetary Science Letters*, *431*, 48–58. https://doi.org/10.1016/j.epsl.2015.09.002

Di Toro, G., Goldsby, D. L., & Tullis, T. E. (2004). Friction falls towards zero in quartz rock as slip velocity approaches seismic rates. *Nature*, *427*(6973), 436–439. https://doi.org/10.1038/nature02249

Di Toro, G., Han, R., Hirose, T., De Paola, N., Nielsen, S., Mizoguchi, K., et al. (2011). Fault lubrication during earthquakes. *Nature*, *471*, 494–498. https://doi.org/10.1038/nature09838

Di Toro, G., Hirose, T., Nielsen, S., Pennacchioni, G., & Shimamoto, T. (2006). Natural and experimental evidence of melt lubrication of faults during earthquakes. *Science*, *331*, 647–649. https://doi.org/10.1126/science.1121012

Di Toro, G., Hirose, T., Nielsen, S., & Shimamoto, T. (2006). Relating high-velocity rock-friction experiments to coseismic slip in the presence of melts. In R. Abercrombie, et al. (Eds.), *Radiated Energy and the Physics of Earthquake Faulting, Geophys. Monogr. Ser*, (Vol. 170, pp. 121–134). Washington, D. C.: AGU. https://doi.org/10.1029/170GM13

Di Toro, G., Niemeijer, A., Tripoli, A., Nielsen, S., Di Felice, F., Scarlato, P., et al. (2010). From field geology to earthquake simulation: a new state-of-the-art tool to investigate rock friction during the seismic cycle (SHIVA). *Rendiconti Lincei*, *21*(1), 95–114. https://doi.org/10.1007/s12210-010-0097-x

Ferré, E. C., Yeh, E.-C., Chou, Y.-M., Kuo, R.-L., Chu, H.-T., & Korren, C. S. (2016). Brushlines in fault pseudotachylytes: a new criterion for coseismic slip direction. *Geology*, *44*(5), 395–398. https://doi.org/10.1130/G37751.1

Fialko, Y., & Khazan, Y. (2005). Fusion by earthquake fault friction: Stick or slip? *Journal of Geophysical Research*, *110*, B12407. https://doi.org/10.1029/2005JB003869

Fluegel, A., Varshneya, A. K., Seward, T. P., & Earl, D. A. (2004). Viscosity ofcommercial glasses in the softening range. In J. R. Varner, T. P. Seward, H. Schaeffer (Eds.), *Proc. Seventh Int. Conf. onAdvances in Fusion and Processing of Glass III* (Vol. 141, pp. 379–86). Westerville, Ohio, USA: The American Ceramic Society. Ceram. Trans

Giordano, D., Russell, J. K., & Dingwell, D. B. (2008). Viscosity of magmatic liquids: a model. *Earth and Planetary Science Letters*, *271*, 123–134. https://doi.org/10.1016/j.epsl.2008.03.038

Goldsby, D. L., & Tullis, T. E. (2011). Flash heating leads to low frictional strength of crustal rocks at earthquake slip rates. *Science*, *334*(6053), 216–218. https://doi.org/10.1126/science.1207902

Green, H. W., Shi, F., Bozhilov, K., Xia, G., & Reches, Z. (2015). Phase transformation and nanometric flow cause extreme weakening during fault slip. *Nature Geoscience*, *8*, 448–489. https://doi.org/10.1038/ngeo2436

Han, R., Hirose, T., & Shimamoto, T. (2010). Strong velocity weakening and powder lubrication of simulated carbonate faults at seismic slip rates. *Journal of Geophysical Research*, *115*, B03412. https://doi.org/10.1029/2008JB006136

Han, R., Shimamoto, T., Hirose, T., Ree, J.-H., & Ando, J. (2007). Ultralow friction of carbonate faults caused by thermal decomposition. *Science*, *316*(5826), 878–881. https://doi.org/10.1126/science.1139763

Hirose, T., & Shimamoto, T. (2003). Fractal dimension of molten surfaces as a possible parameter to infer the slip-weakening distance of faults from natural pseudotachylites. *Journal of Structural Geology*, *25*, 1569–1574. https://doi.org/10.1016/S0191-8141(03)00009-9

Hirose, T., & Shimamoto, T. (2005). Growth of molten zone as a mechanism of slip weakening of simulated faults in gabbro during frictional melting. *Journal of Geophysical Research*, *110*, B05202. https://doi.org/10.1029/2004JB003207

Kitano, T., Kataoka, T., & Shirota, T. (1981). An empirical equation of the relative viscosity of polymer melts filled with various inorganic fillers. *Rheologica Acta*, *20*, 207–209. https://doi.org/10.1007/BF01513064

Korren, C. S., Ferré, E. C., Yeh, E.-C., Chou, Y.-M., & Chu, H.-T. (2016). Seismic rupture parameters deduced from a Pliocene fault pseudotachylyte in Taiwan. In M. Y. Thomas, T. M. Mitchell, & H. S. Bhat (Eds.), *Fault Zone Dynamic Processes: Evolution of Fault Zone Properties and Dynamic Processes During Seismic Rupture AGU Monograph*, (p. 21–35). Washington, USA: American Geophysical Union. https://doi.org/10.1002/9781119156895.ch2

Kuo, L.-W., Hsiao, H. C., Song, S.-R., Sheu, H. S., & Suppe, J. (2014). Coseismic thickness of principal slip zone from the Taiwan Chelungpu fault Drilling Project-A (TCDP-A) and correlated fracture energy. *Tectonophysics*, *619–620*, 29–35. https://doi.org/10.1016/j.tecto.2013.07.006

Kuo, L.-W., Li, H., Smith, S., Di Toro, G., Suppe, J., Song, S. R., et al. (2014). Gouge graphitization and dynamic fault weakening during the 2008 Mw 7.9 Wenchuan earthquake. *Geology*, *42*, 47–50. https://doi.org/10.1130/G34862.1

Kuo, L.-W., Song, S.-R., Huang, L., Yeh, E.-C., & Chen, H.-F. (2011). Temperature estimates of coseismic heating in clay-rich fault gouges, the Chelungpu fault zones, Taiwan. *Tectonophysics*, *502*, 315–327. https://doi.org/10.1016/j.tecto.2011.02.001

Kuo, L.-W., Song, Y.-F., Yang, C.-M., Song, S.-R., Wang, C.-C., Dong, J.-J., et al. (2015). Ultrafine spherical quartz formation during seismic fault slip: Natural and experimental evidence and its implications. *Tectonophysics*, *664*, 98–108. https://doi.org/10.1016/j.tecto.2015.09.008

Kuo, R.-L. (2016). Microstructural and Magnetic Investigations of Pseudotachylyte and Ultracataclasite in the Hoping River, Tananao Complex, Eastern Taiwan. Unpubl. M.Sc. thesis, National Taiwan University, Taipei, Taiwan, R.O.C.

Lavallée, Y., Mitchell, T. M., Heap, M. J., Vasseur, J., Hess, K.-U., Hirose, T., & Dingwell, D. B. (2012). Experimental generation of volcanic pseudotachylyte: constraining rheology. *Journal of Structural Geology*, *38*, 222–233. https://doi.org/10.1016/j.jsg.2012.02.001

Lee, S. K., Han, R., Kim, E. J., Jeong, G. Y., Khim, H., & Hirose, T. (2017). Quasi-equilibrium melting of quartzite upon extreme friction. *Nature Geoscience*, *10*, 436–441. https://doi.org/10.1038/ngeo2951

Lejeune, A. M., Bottinga, Y., Trull, T. W., & Richet, P. (1999). Rheology of bubble-bearing magmas. *Earth and Planetary Science Letters*, *166*, 71–84. https://doi.org/10.1016/S0012-821X(98)00278-7

Manga, M., Castro, J., Cashman, K. V., & Loewenberg, M. (1998). Rheology of bubble-bearing magmas. *Journal of Volcanology and Geothermal Research*, *87*, 15–28. https://doi.org/10.1016/S0377-0273(98)00091-2

Metzner, A. B. (1985). Rheology of suspensions in polymeric liquids. *Journal of Rheology*, *29*, 739–775. https://doi.org/10.1122/1.549808

Nielsen, S., Di Toro, G., Hirose, T., & Shimamoto, T. (2008). Frictional melt and seismic slip. *Journal of Geophysical Research*, *113*, B01308. https://doi.org/10.1029/2007JB005122

Nielsen, S., E. Spagnuolo, and M. Violay (2012), The ultimate sample preparation for rotary shear experiments. Rapporti tecnici INGV, (http://istituto.ingv.it/l-ingv/produzione-scientifica/rapporti-tecnici-ingv/numeri-pubblicati-2012).

Niemeijer, A., Di Toro, G., Griffith, W. A., Bistacchi, A., Smith, S. A., & Nielsen, S. (2012). Inferring earthquake physics and chemistry using an integrated field and laboratory approach. *Journal of Structural Geology*, *39*, 2–36. https://doi.org/10.1016/j.jsg.2012.02.018

Niemeijer, A., Di Toro, G., Nielsen, S., & Di Felice, F. (2011). Frictional melting of gabbro under extreme experimental conditions of normal stress, acceleration, and sliding velocity. *Journal of Geophysical Research*, *116*, B07404. https://doi.org/10.1029/2010JB008181

Passelègue, F. X., Spagnuolo, E., Violay, M., Nielsen, S., Di Toro, G., & Schubnel, A. (2016). Frictional evolution, acoustic emissions activity, and off-fault damage in simulated faults sheared at seismic slip rates. *Journal of Geophysical Research: Solid Earth*, *121*, 7490–7513. https://doi.org/10.1002/2016JB012988

Proctor, B. P., Mitchell, T. M., Hirth, G., Goldsby, D., Zorzi, F., Platt, J. D., & Di Toro, G. (2014). Dynamic weakening of serpentinite gouges and bare surfaces at seismic slip rates. *Journal of Geophysical Research: Solid Earth*, *119*, 8107–8131. https://doi.org/10.1002/2014JB011057

Reches, Z., & Lockner, D. A. (2010). Fault weakening and earthquake instability by powder lubrication. *Nature*, *467*(7314), 452–455. https://doi.org/10.1038/nature09348

Rice, J. R. (2006). Heating and weakening of faults during earthquake slip. *Journal of Geophysical Research*, *111*, B05311. https://doi.org/10.1029/2005JB004006

Rowe, C., Lamothe, K., Rempe, M., Andrews, M., Mitchell, T., Di Toro, G., et al. (2019). Earthquake lubrication and healing explained by amorphous nanosilica. *Nature Communications*, *10*(1), 320. https://doi.org/10.1038/s41467-018-08238-y

Shand, S. J. (1916). The pseudotachylyte of Parys. *Geological Society of London*, *72*, 198–221. https://doi.org/10.1144/GSL.JGS.1916.072.01-04.12

Shimamoto, T., & Nagahama, H. (1992). An argument against the crush origin of pseudotachylytes based on the analysis of clast-size distribution. *Journal of Structural Geology*, *14*, 999–1006. https://doi.org/10.1016/0191-8141(92)90031-Q

Shimamoto, T., & Tsutsumi, A. (1994). A new rotary-shear high-speed frictional testing machine: Its basic design and scope of research. *Journal of Tectonic Research Group of Japan*, *39*, 65–78. (in Japanese with English abstract)

Sibson, R. H. (1975). Generation of pseudotachylyte by ancient seismic faulting. *Geophysical Journal International*, *43*(3), 775–794. https://doi.org/10.1111/j.1365-246X.1975.tb06195.x

Song, S. R., Kuo, L. W., Yeh, E. C., Wang, C. Y., Hung, J. H., & Ma, K. F. (2007). Characteristics of the lithology, fault-related rocks and fault zone structures in the TCDP Hole-A. *Terrestrial, Atmospheric and Oceanic Sciences*, *18*, 243–269. https://doi.org/10.3319/TAO.2007.18.2.243(TCDP)

Song, Y. F., Chang, C. H., Liu, C. Y., Chang, S. H., Jeng, U. S., Lai, Y. H., et al. (2007). X-ray beamlines for structural studies at the NSRRC superconducting wavelength shifter. *Journal of Synchrotron Radiation*, *14*(4), 320–325. https://doi.org/10.1107/S0909049507021516

Spagnuolo, E., Plümper, O., Violay, M., Cavallo, A., & Di Toro, G. (2015). Fast-moving dislocations trigger flash weakening in carbonate-bearing faults during earthquakes. *Scientific Reports*, *5*, 1–11. https://doi.org/10.1038/srep16112

Spray, J. G. (1987). Artificial generation of pseudotachylyte using friction welding apparatus: Simulation of melting on a fault plane. *Journal of Structural Geology*, *9*, 49–60. https://doi.org/10.1016/0191-8141(87)90043-5

Spray, J. G. (1995). Pseudotachylyte controversy: fact or friction. *Geology*, *23*, 1119–1122. https://doi.org/10.1130/0091-7613(1995)023<1119:PCFOF>2.3.CO;2

Spray, J. G. (2005). Evidence for melt lubrication during large earthquakes. *Geophysical Research Letters*, *32*, L07301. https://doi.org/10.1029/2004GL022293

Spray, J. G. (2010). Frictional melting processes in planetary materials: from hyper-velocity impacts to earthquakes. *Annual Review of Earth and Planetary Sciences*, *38*, 221–254. https://doi.org/10.1146/annurev.earth.031208.100045

Steinike, U., & Tkáčová, K. (2000). Mechanochemistry of Solids—Real Structure and Reactivity. *Journal of Materials Synthesis and Processing*, *8*, 197. https://doi.org/10.1023/A:1011364110355

Tsutsumi, A. (1999). Size distribution of clasts in experimentally produced pseudotachylytes. *Journal of Structural Geology*, *21*, 305–312. https://doi.org/10.1016/S0191-8141(98)00113-8

Violay, M., Di Toro, G., Nielsen, S., Gibert, B., Spagnuolo, E., Azais, P., & Scarlato, P. G. (2014). Effect of glass on the frictional behavior of basalts at seismic slip rates. *Geophysical Research Letters*, *41*, 348–355. https://doi.org/10.1002/2013GL058601

Violay, M., Nielsen, S., Gibert, B., Spagnuolo, E., Cavallo, A., Azais, P., et al. (2014). Effect of water on the frictional behavior of cohesive rocks during earthquakes. *Geology*, *42*(1), 27–30. https://doi.org/10.1130/G34916.1

Violay, M., Passelegue, F., Spagnuolo, E., Di Toro, G., & Cornelio, C. (2019). Effect of water and rock composition on re-strengthening of cohesive faults during the deceleration phase of seismic slip pulses. *Earth and Planetary Science*, *522*, 55–64. https://doi.org/10.1016/j.epsl.2019.06.027

Wallace, P. A., De Angelis, S. H., Hornby, A. J., Kendrick, J. E., Clesham, S., von Aulock, F. W., et al. (2019). Frictional melt homogenisation during fault slip: Geochemical, textural and rheological fingerprints. *Geochimica et Cosmochimica Acta*, *255*, 265–288. https://doi.org/10.1016/j.gca.2019.04.010

Yang, C. H., Yu, W.-L., Dong, J.-J., Kuo, C.-Y., Shimamoto, T., Lee, C.-T., et al. (2014). Initiation, movement, and run-out of the giant Tsaoling landslide — what can we learn from a simple rigid block model and a velocity–displacement dependent friction law? *Engineering Geology*, *182*, 158–181. https://doi.org/10.1016/j.enggeo.2014.08.008

Yin, G.-C., Song, Y.-F., Tang, M.-T., Chen, F.-R., Liang, K. S., Duewer, F. W., et al. (2006). 30 nm resolution X-ray imaging at 8 keV using third order diffraction of a zone plate lens objective in a transmission microscope. *Applied Physics Letters*, *89*. https://doi.org/10.1063/1.2397483